Versatile three-dimensional denoising and segmentation method of X-ray tomographic images: applications to geomaterials characterizations

Olivier Rozenbaum, Maïtine Bergounioux, António Maurício, Carlos Figueiredo, Carlos Alves, Luc Barbanson

Versatile three-dimensional denoising and segmentation method of X-ray tomographic images: applications to geomaterials characterizations

**Olivier Rozenbaum, Maïtine Bergounioux,
António Maurício, Carlos Figueiredo, Carlos
Alves, Luc Barbanson**

Abstract For most issues encountered in materials sciences and in geosciences, X-ray microtomography is an efficient technique to obtain morphological, structural, and topological information on complex multiphasic materials. However the segmentation of three-dimensional images of these materials is rarely straightforward. For instance, the segmentation processes that are used are strongly dependant on the quality of the images, the samples and the objects or phases of interest to extract. In this study a variational method which is a versatile technique enabling to segment a lot of three-dimensional images of geomaterials has been developed. This technique is illustrated with two case studies belonging to two distinct fields of research in earth sciences. In one case the crack network of a weathered granite sample is considered, while, in the other, the distributions of the mineralogical phases on an ore sample are investigated.

Olivier Rozenbaum and Luc Barbanson
ISTO, Université d'Orléans, CNRS, BRGM, 1A rue de la Ferollerie, 45100, Orléans cedex 2, France
E-mail: Rozenbaum@cnrs-orleans.fr and luc.barbanson@univ-orleans.fr

Maïtine Bergounioux
Université d'Orléans, Math., Labo. MAPMO, UMR 7349, Federation Denis Poisson, BP 6759, 45067 Orléans cedex 2
E-mail: Maitine.Bergounioux@univ-orleans.fr

António Maurício and Carlos Figueiredo
Centro de Recursos Naturais e Ambiente (CERENA), Instituto Superior Técnico, Av. Rovisco Pais, 1049-001 Lisboa, Portugal
E-mail: pcd2045@ist.utl.pt and carlos.m.figueiredo@ist.utl.pt

Carlos Alves
Lab2PT, Landscape, Heritage and Territory Laboratory (Research unit of the Portuguese Fundação para a Ciência e a Tecnologia, UID/AUR/04509/2013) and School of Sciences, University of Minho, Braga, Portugal
E-mail: casaix@dct.uminho.pt

1 Introduction

X-ray microtomography (μ-CT) is a non-destructive imaging technique, which enables the study of materials internal microstructure. On a μ-CT scanner, a sample is placed on a rotary stage between an X-ray source and a flat panel detector. Basically, the sample is illuminated by the X-ray beam and its projections are recorded on the detector.

During acquisition, the sample is rotated step by step, taking a projection image at each angular position. The projection set is used as an input for the image reconstruction algorithm. This is done by using a filtered back projection algorithm: a computer reconstructs from the projections the cross-sectional images of the sample (called tomograms). Stacking these reconstructed images forms a three-dimensional image of the sample (volume dataset). At each voxel space position of the resulting dataset, a grey-value corresponds to the effective X-ray attenuation coefficient. Therefore, if the principal compounds of the object are known and have a sufficient density contrast, the distribution of these compounds within the object can be easily deduced. Unfortunately, this is not often the case as illustrated in the following with two different geomaterials.

With a polychromatic X-ray beam, which is the case for laboratory μ-CT, artifacts are inevitable and difficult to remove. It is therefore difficult to lay voxel values with material densities in an absolute and quantitative manner. Frequently encountered artifacts include: beam hardening effect [27] where an object of uniform density appears to have a thick and dense skin or ring effect [16], generally caused by temporary and spurious bad pixels in the detector. These effects can be reduced by the reconstruction method, but only to a certain extent and is less effective for multi-component objects.

From a practical point of view, the acquired images have a sufficient resolution to catch all the features of interest (e.g. pores, cracks etc.). However, the X-ray acquisition process always induces a consequent noise. In the context of studying material structure this is quite challenging to get rid of the noise while keeping the structural and morphological information (solid phases, pore phase, interfaces separating these phases) that may be at the same scale order as the noise. In other words, there is a necessity to obtain convenient mathematical tools to segment three-dimensional images of complex materials in order to extract the different phases. Classical denoising methods as gaussian or morphological low-pass filters are not always suitable since they strongly erode, blur and/or smooth contours. As an alternative, filtering processes based on variational methods have been developed during the past decade. They are based on the first order Rudin-Osher-Fatemi model (ROF) [19]. This model

is based on the fact that the observed image f may be written as $f = f_0 + w$ where f_0 is the denoised image and w the noise (usually assumed to be a gaussian one). So far, priors on f_0 give a solution more or less piecewise constant. An often encountered drawback is the so-called "staircasing" effect: artificial (and of course unwanted) contours appear. This is generally not suitable for segmentation.

In [8] a second order model (called (ROF2) in the following) was presented where the (first order) prior term was replaced by a second order one using an appropriate mathematical framework. The use of such a model allows to get rid of the staircasing effect. However, it has been noticed that while the staircasing effect disappeared, the resulting image was slightly blurred (the blur effect was not as important as if a classical low-pass filter has been used however) since solutions are now piecewise affine. Therefore, the model in [9] have been improved performing a finer decomposition of the denoised image f_0 = contours (u) + dynamic or smooth *coloured* part(v) so that $f = u + v + w$ to get rid of this effect as well.

The paper is organized as follows. The fields of research concerned in this article are explained and the two geomaterials investigated by X-ray microtomography are presented (section 2). Then, the preprocessing decomposition model that will allow to perform sharp analysis of the material structure in section 3 is explained. Section 4 is devoted to describing the whole image processing and numerical results. In the last section, some comments about the two geomaterial structures are given. This will be achieved considering, namely a granite stone and an ore. For each casen, the issues and what image preprocessing provides are shortly presented. Then a quantitative analysis to get structural and morphological information as, for instance, porosity and chord length distributions is performed.

2 The geological context

2.1 Acquisition context

Microtomography analysis presented in this article was performed using an industrial CT device Nanotom 180NF (GE Phoenix—X-ray, Wunstorf, Germany) available at the ISTO. This unit has a 180kV nanofocus X-ray tube and a digital detector array (2304×1152 pixels Hamamatsu detector). Samples were placed in the chamber and rotated by 360 degrees during acquisition. The resulting projections were converted into a three-dimensional image stack using a microcluster of four PCs with the Phoenix three-dimensional reconstruction software (filtered back projection Feldkamp algorithm [12]. The reconstruction software contains several different modules for artifact reduction (e.g. beam hardening, ring artifacts) to optimize the results. Finally, the 16-bit three-dimensional image was converted into 8-bit (256 grey levels) for the image analysis processing.

In order to obtain high penetrating X-ray a target made of tungsten was selected. The samples (in the form of 6 mm diameter rods) were mounted and waxed on a carbon fibre rod. For the granite sample (section 2.2) an operating voltage of 110 kV and a filament current of 59 μA were applied. The distance between the X-ray source and the sample and between the X-ray source and the detector was 16 and 500 mm, respectively, giving a voxel size of 3.2 μm. The 2000 projection images (angular increment of 0.18^o) were acquired during stone rotation (with an acquisition time of 4 hours). For the ore sample (section 2.3) an operating voltage of 160 kV and a filament current of 23 μA were applied. The distance between the X-ray source and the sample and between the X-ray source and the detector was 16 and 500 mm, respectively, giving a voxel size of 3.2 μm. The 1800 projection images (angular increment of 0.20^o) were acquired during ore sample rotation (with an acquisition time of 3.5 hours).

2.2 Granite sample

The study of this stone takes place in a cultural heritage context. Building stones of heritage monuments suffer their climatic environment and are often altered and eventually destroyed. This phenomenon called *weathering* is present in all the countries around the world and many studies are led to slow down, control or avoid this decay [25,3,22]. In this context, a building granite stone originating from a portuguese monument is studied.

The Braga granite is a porphyritic two-mica granite, biotite-rich, fine to medium grained [13] frequently found in the monuments of Braga (NW Portugal) and that present diverse erosive features related to salt contamination [1,2,17]. In the weathering profiles of the Braga granite there are blocks of bluish-grey color that, following the conventions of field descriptions [14], can be considered as fresh rock. The weathering front develops along the joint network and it is marked macroscopically by the yellowing of the rock, being also accompanied by mineralogical transformations to weathering products such as kaolinite and gibbsite [24]. Petrophysical studies showed that the unweathered rock is less porous with lower capillary migration coefficients than the weathered type [1]. In the historical buildings of Braga, bluish-grey stones of this Braga granite rarely present erosive decay (when present are generally of small expression), while erosive features (plates, flakes and granular disintegration are more frequent and expressive in the yellowish stones [1,17]. Petrographic studies of resin imbibed thin sections of the Braga granite allowed to discuss the relation between porosity structures and petrographic features [1]. In the fresh bluish-grey rock type, porosity is dominated by pores inside the plagioclase crystals that were interpreted to be related to hydrothermal alteration processes (considering the associated alteration minerals) and, in a lesser extent, to some fine inter and intragranular fissures. In the weathered but still stone-like rock, there is an important development of intragranular

porosity in the plagioclase crystals that was attributed to weathering of this mineral (with formation of kaolinite and gibbsite). It is also observed the occurrence of an important network of inter, intra and transgranular fissures. The aim of this study for this weathered granite sample is to extract the crack network from three-dimensional images. This will enable in a first step to obtain topological information and evaluate in future studies water transfer properties of this stone.

2.3 Ore sample

On one hand, the study is peformed from a pure geological point of view i.e. the comprehension of minerals formation as explained in the sequel On the other hand, the study aims at quantify the distribution of these minerals in a mining context and optimize the mineral processing.

The ore sample was collected in the Reocin mine in the North of Spain [4]. The Reocin Zn – (Pb) deposit is a Mississippi Valley Type one, hosted by Cretaceous dolomite rock, where mineralization is compound, in decreasing order of abundance, by: sphalerite (ZnS), galena (PbS), marcasite (FeS_2), Fe-dolomite ($(Fe,Mg)Ca(CO_3)_2$) and dolomite ($MgCa(CO_3)_2$). This ore is a mineralized internal sediment where sphalerite and a minor amount of the others sulphides are distributed in parallel ribbons within a dolomitic matrix. As sphalerite is largely the dominant sulfide, it is only refer to this mineral in the following. The grains of sphalerite are euhedral crystals whereas carbonate appears as xenomorphic grains. Within a single ribbon, the content in sphalerite decreases from top to bottom. The sulphide ribbons exhibit a Liesegang ring pattern. Indeed, in the studied ore sample, sphalerite is distributed in parallel bands. Such pattern can be interpreted as resulting from a process of diffusion within a porous medium, given this structure known as Liesegang rings [28].

Qualitative observations of Liesegang rings address the process of formation of the mineralization, but, a better understanding of this process require a quantitative description of the mineral microstructure. For example, the reference to the Lisesegang's pattern suggests that sphalerite precipitation could involve the mixing of two solutions (one rich in reduced sulphur, the other Zn-rich) flowing in opposite directions within a porous medium. In this case, according to the theory of the Liesegang pattern, the distance between ribbons is a simple function of diffusive coefficients and thus, testing the possibility of referring to the Liesengang process needs a quantitative study of the microstructure of the mineralization. The aim of this study for the ore sample is to extract the sphalerite phase from the dolomite phase (from three-dimensional images) and determine some characteristics of the ore (e.g. volume fraction of each constituent).

Moreover, the first stage of extracting metal from ore is a grinding operation. The objective of this latter is to create fragments ideally composed either by valuable mineral (sphalerite), or by gangue mineral (dolomite). The size of the fragment for which such a situation is obtained is called the liberation size. The liberation size is a function of the granularity of valuable mineral. As grinding operations are of poor energetic efficiency, obtaining the liberation size implies a great consumption of energy and the cost of this stage is a strong constraint in assessing the economic viability of a mining project. Thus, granulometric studies of valuable mineral are a step in accessing the economic cost of liberation. This will be estimated in future attempts from the three-dimensional images by Voronoi tiling [23].

3 A pre-processing image decomposition model

The information to recover is different according to the considered images: for instance, the goal to achieve for the granite sample is the cracks identification while the one for the ore sample is the mineral phases distributions. In addition, the segmentation process is difficult to perform but not for the same reasons: it strongly depends on the image (and thus on the samples, since the acquisition is the same). A preprocessing treatment able to highlight particular image features is needed. A variational decomposition model is proposed in this article and briefly presented in the sequel (for more details the reader can refer to [6,7]). Shortly speaking, this model assume that the observed image f can be split into three components: a smooth part v that contains the image dynamics (light for instance, mean grey level), a part u that is expected to contain the main contours and should be piecewise constant and an oscillating part w that should involve noise and/or fine textures. A variational model is used, namely

$$\inf_{(u,v,w)} \left\{ \mathscr{J}(u,v,w),\ u+v+w=f \right\},$$

where $\mathscr{J}$ is an "energy" functional that is described next. For the sake of simplicity a two dimensional model is presented, but a three-dimensional model was implemented and the numerical experiments were performed for three-dimensional stacks of grey level images. The complete description of the three-dimensional algorithm is described in [5,26].

3.1 Discretization process

It is assumed that the image is rectangular with size $N \times M$. Let $X := \mathbb{R}^{N \times M} \simeq \mathbb{R}^{NM}$ endowed with the usual inner product and the associated euclidean norm

$$\langle u, v \rangle_X := \sum_{1 \le i \le N} \sum_{1 \le j \le M} u_{i,j} v_{i,j}, \quad \|u\|_X := \sqrt{\sum_{1 \le i \le N} \sum_{1 \le j \le M} u_{i,j}^2}. \qquad (3.1)$$

Setting $Y = X \times X$. It is classical to define the discrete total variation with finite difference schemes : the discrete gradient of the numerical image $u \in X$ is $\nabla u \in Y$ computed by the forward scheme for example:

$$(\nabla u)_{i,j} = \left((\nabla u)_{i,j}^1, (\nabla u)_{i,j}^2 \right), \tag{3.2}$$

where

$$(\nabla u)_{i,j}^1 = \begin{cases} u_{i+1,j} - u_{i,j} & \text{if } i < N \\ 0 & \text{if } i = N, \end{cases} \text{ and } (\nabla u)_{i,j}^2 = \begin{cases} u_{i,j+1} - u_{i,j} & \text{if } j < M \\ 0 & \text{if } j = M. \end{cases}$$

Set

$$J_1(u) = \sum_{1 \le i \le N} \sum_{1 \le j \le M} \sqrt{\left(\nabla u_{i,j}^1 \right)^2 + \left(\nabla u_{i,j}^2 \right)^2} \tag{3.3}$$

as the discrete form of the total variation :

$$J_1(u) \simeq \int_{\Omega} |\nabla u| \, dx,$$

where Ω is the image domain and

$$J_2(v) = \sum_{1 \le i \le N} \sum_{1 \le j \le M} \sqrt{(Hv_{i,j}^{11})^2 + (Hv_{i,j}^{12})^2 + (Hv_{i,j}^{21})^2 + (Hv_{i,j}^{22})^2}, \tag{3.4}$$

where, the Hessian matrix of v, denoted Hv is identified to a X^4 vector:

$$\forall v \in X \quad (Hv)_{i,j} = \left((Hv)_{i,j}^{11}, (Hv)_{i,j}^{12}, (Hv)_{i,j}^{21}, (Hv)_{i,j}^{22} \right),$$

with, for every $i, j = 1, \ldots, N,$

$$(Hv)_{i,j}^{11} = \begin{cases} v_{i+1,j} - 2v_{i,j} + v_{i-1,j} & \text{if } 1 < i < N, \\ v_{i+1,j} - v_{i,j} & \text{if } i = 1, \\ v_{i-1,j} - v_{i,j} & \text{if } i = N, \end{cases}$$

$$(Hv)_{i,j}^{12} = \begin{cases} v_{i,j+1} - v_{i,j} - v_{i-1,j+1} + v_{i-1,j} & \text{if } 1 < i \le N, \, 1 \le j < N, \\ 0 & \text{if } i = 1, \\ 0 & \text{if } i = N, \end{cases}$$

$$(Hv)_{i,j}^{21} = \begin{cases} v_{i+1,j} - v_{i,j} - v_{i+1,j-1} + v_{i,j-1} & \text{if } 1 \le i < N, \, 1 < j \le N, \\ 0 & \text{if } i = 1, \\ 0 & \text{if } i = N, \end{cases}$$

$$(Hv)_{i,j}^{22} = \begin{cases} v_{i,j+1} - 2v_{i,j} + v_{i,j-1} & \text{if } 1 < j < N, \\ v_{i,j+1} - v_{i,j} & \text{if } j = 1, \\ v_{i,j-1} - v_{i,j} & \text{if } j = N. \end{cases}$$

J_2 is the discrete form of the second order total variation. The problem writes

$$\inf_{(u,v) \in X \times X} \frac{1}{2} \|f - u - v\|_X^2 + \lambda J_1(u) + \mu J_2(v). \tag{3.5}$$

where $\lambda > 0$, and $\mu > 0$.

3.2 Numerical realization and algorithm

Let (u^*, v^*) be the unique solution to Eq. (3.5). Define K_1 and K_2 as the following convex closed subsets :

$$K_1 = \{\text{div } p \mid p \in X^2, \ \|p_{i,j}\|_{\mathbb{R}^2} \leq 1 \ \forall i = 1, \ldots, N, j = 1, \ldots, M\}, \qquad (3.6a)$$

$$K_2 = \{H^* p \mid p \in X^4, \ \|p_{i,j}\|_{\mathbb{R}^4} \leq 1, \ \forall i = 1, \ldots, N, j = 1, \ldots, M\}, \qquad (3.6b)$$

where the discrete divergence operator -div is the adjoint operator of the gradient operator ∇ and H^* the adjoint of H. Let Π_K be the orthogonal projection on a generic closed convex set K. The following fixed-point algorithm is used to compute the solution:

Algorithm 1

Initialization step. Choose $u_0 = 0$ and $v_0 = 0$ and $0 < \alpha < 1/2$.

Iteration n : Define the sequences $((u_n, v_n))_n$ as

$$\begin{cases} u_{n+1} = u_n + \alpha \left(f - u_n - v_n - \Pi_{\lambda K_1} (f - v_n) \right) \\ v_{n+1} = v_n + \alpha \left(f - u_{n+1} - v_n - \Pi_{\mu K_2} (f - u_{n+1}) \right). \end{cases}$$

Stopping criterion.

If $\alpha \in (0, 1/2)$, the sequence generated by algorithm Eq. (3.2) converges to the solution. The two projections $\Pi_{\lambda K_1}$ and $\Pi_{\lambda K_2}$ are computed as in [8,9,26] using either a Nesterov algorithm [18,29] or the primal-dual algorithm of Chambolle and Pock [10].

4 Numerical tests

Tests have been performed on multicore computers using parallelized C^{++} code. The three-dimensional algorithm has been used but the method is presented and commented on a slice for the sake of simplicity. However, the main challenge of variational methods (including the one used here of course) is the parameter tuning. Some comments and numerical analysis have been performed in [7]. The pre-processing step has to be tuned by hand for the moment. Nevertheless, once the parameters have been checked on one slice, the same values have been used for the three-dimensional stack.

Granite sample is processed with parameters $\lambda \simeq \mu$; then one focused on the so called *cartoon* part u that contains the main contours and perform a thresholding to achieve the contour segmentation. The ore sample is easier to handle since a denoising process only have to be performed while preserving contours. Hence, the component $u + v$ is used in this case. In the following, the use of the method with respect to the sample type is detailed.

4.1 Granite sample

Figure 4.1 illustrates the decomposition process: the original image (Fig. 4.1 (a)) is split in 3 components (setting $\lambda = 10$ and $\mu = 15$). As already mentioned, the interesting component is the contour one (u reported in Fig. 4.1 (c)). Hence, the image dynamic (Fig. 4.1 (b)) and the noise (Fig. 4.1 (d)) are ruled out.

(a) Original image   (b) part v (dynamics)

(c) part u (contours)   (d) part w (noise)
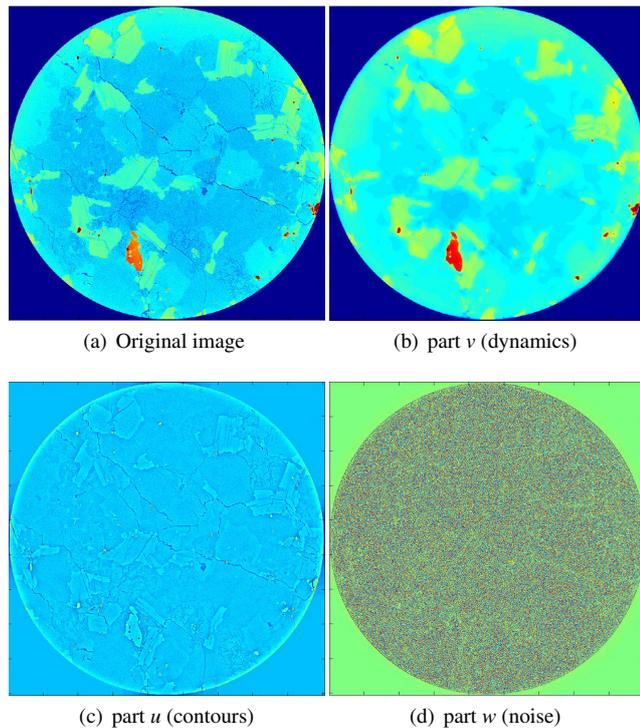
Fig. 4.1 Decomposition process (sample diameter=6mm) .

Once the decomposition is done, the crack identification is achieved performing a thresholding step on the part u. More precisely, the thresholded image is u_s

$$u_s = \begin{cases} 0 \text{ on } \{u < m(u)\} \\ 1 \text{ else,} \end{cases}$$

where $m(u)$ is the mean value of u. This is reported on Fig. 4.2 and Fig. 4.3 gives the result of the decomposition for the three-dimensional stack.

(a) part *u* (contours)   (b) Thresholding
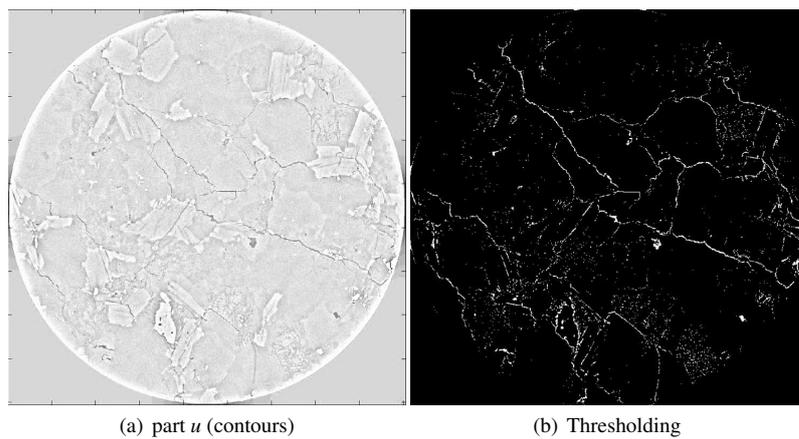
Fig. 4.2 Denoising and segmentation process (sample diameter=6mm) .

(a) Original Image   (b) part -*u*

(c) part *v*   (d) part *w*
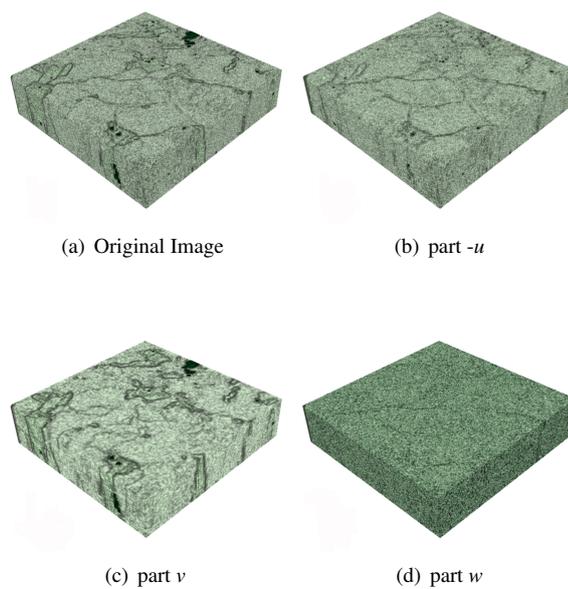
Fig. 4.3 Decomposition of a three-dimensional X-ray stack (subvolume=3.2x3.2x0.8 mm^3) .

In the thresholded image (Fig. 4.2 (b)) micro-cracks with some residual noise are distinguished among long cracks (macro-structures). If the result is not satisfactory, it is possible to end the process using some wavelet filter to remove this residual

noise (a median filter is not efficient here). However, one of our main interests is the identification of the micro-cracks and some of these latter have sizes less (or equal) than the pixel size image. Hence, there is a priori no way to get rid of the residual noise while preserving those tiny structures. It can be noticed that some macro-structures are disconnected because the micro-cracks have been partly lost during the denoising process (Fig. 4.2 (b)). Nevertheless, these micro-structures are involved in the residual w part (see Fig. 4.1 (d) where the cracks are still visible). Next challenge is to separate the noise (which is purely random) from the micro-structures. Probabilistic methods are currently investigated to achieve this goal and recover structured voxels in (unstructured) noise. This work is actually in progress. Note that an alternative method is to perform a rescaling using tomographic images from a smaller sample with higher resolution, but this requires additional acquisition.
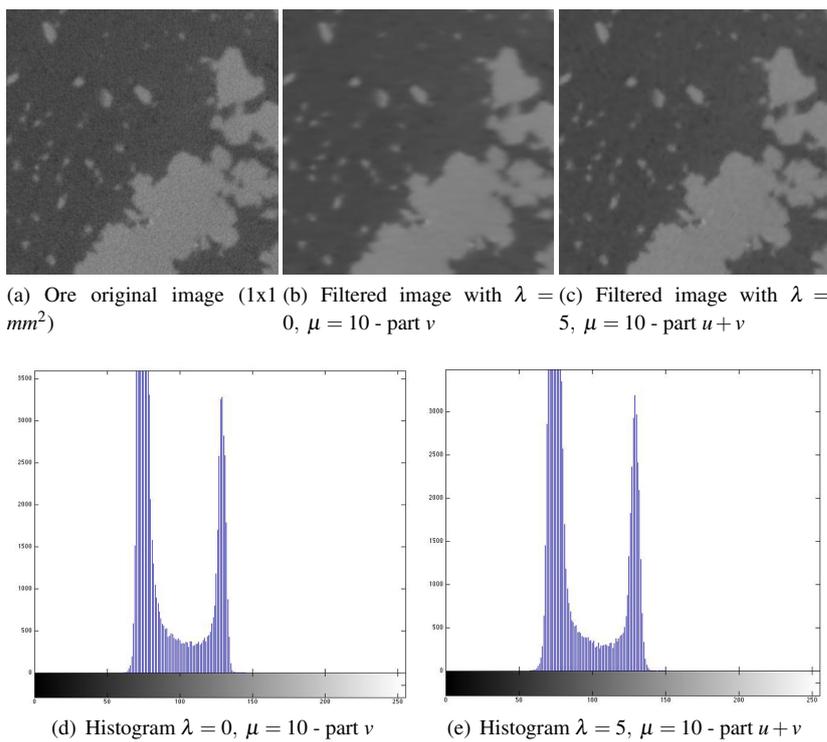
Once the three-dimensional image is binarized and the objects of interest numerically distinguished, morphological and/or textural analysis can be done. For this weathered granite, the porous network of cracks has a relatively low total porosity (2.4%). It represents the porosity accessible for the image resolution (voxel size=3.2 μm). Hence, this value cannot include the porosity of the finest pores (or cracks) such as those related to the intense weathering of the plagioclase. The spatial repartition of this network is particularly anisotropic as illustrated in Fig. 4.4. For sake of clarity, only the open porosity is represented in Fig. 4.4 or, in other words, the percolating porous network. This was done by removing all the isolated micro-pores non-connected to this percolating porous network. This choice is also justified by assuming that significant water transfer can occur only through this percolating network. Indeed, these cracks are expected to be the main connected capillary porous network, enabling water to be sucked into the interior of the stone. And as it is well known in the field of cultural heritage, water transfer is one of the main factors involved in stone weathering. Future research will be focused on this percolating network, notably to evaluate stone permeability directly from these images via a lattice Boltzmann simulation [11].
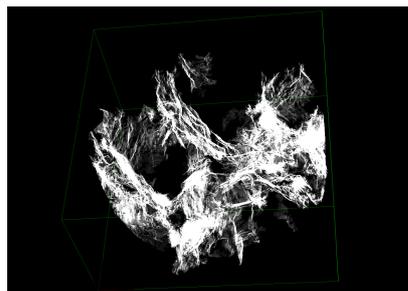
Fig. 4.4 A perspective of the three-dimensional crack network extracted from a granite rod sample (diameter=5.4 mm, height=3.2 mm).
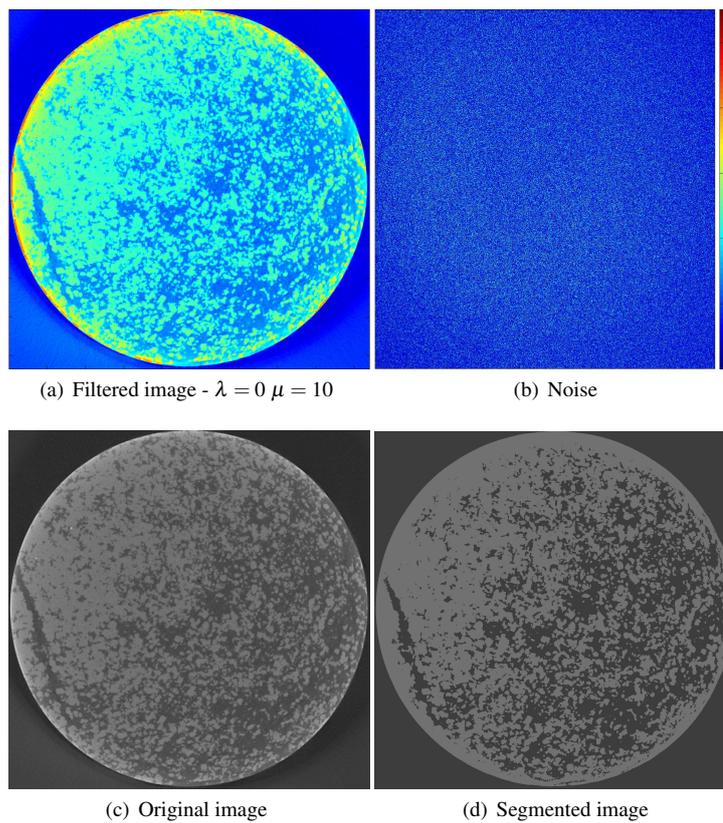
4.2 Ore sample

The problematic is not the same concerning these images. A region classification (and segmentation) has to be performed to obtain the precise two phases distribution. However, these images are very noisy so that classical methods cannot be applied without a preliminary denoising process. Here, the previous model is used to get the denoised image using $u + v$. Indeed, a three parts splitting have no interest since the objective is to get ride of the noise while preserving the contours. A classical first order method ($\mu = 0$) could be used but a *staircasing effect* (additional fictitious contours) may occur. However, the results obtained using the $u + v$ part (Fig. 4.5 (c) and (e)) are compared with the ones obtained using only the u part with $\lambda = 0$ (Fig. 4.5 (b) and (d)). It can be noticed that the results are similar and are good enough for our purpose. Indeed, the full decomposition is time consuming while the choice $\lambda = 0$ need far less computation time. Moreover, in this case the tuning of the parameter μ is much easier and can be done automatically if the noise level is known a priori. Nevertheless, a blind method is easy to manage and is robust with respect to the choice of μ (that should be chosen large enough).

(a) Ore original image (1x1 mm^2) (b) Filtered image with $\lambda = 0$, $\mu = 10$ - part v (c) Filtered image with $\lambda = 5$, $\mu = 10$ - part $u + v$

(d) Histogram $\lambda = 0$, $\mu = 10$ - part v

(e) Histogram $\lambda = 5$, $\mu = 10$ - part $u + v$

Fig. 4.5 Denoising process: comparison between the full decomposition model with $\lambda = 5$, $\mu = 10$ and the partial one $\lambda = 0$, $\mu = 10$. The two histograms are presented as the segmentation method is based on them.

Figure 4.6 illustrates the process : (a) is the filtered image using a second-order variational filter (that prevents from staircasing effects and artificial contours generation) with $\mu = 10$. Image (b) is the removed noise. Once denoising has been performed, the Otsu method [20] have been used with $k = 2$ regions, to identify the regions of interest. Images (c) and (d) illustrates the result.

(a) Filtered image - $\lambda = 0\ \mu = 10$ (b) Noise

(c) Original image   (d) Segmented image

Fig. 4.6 Denoising and segmentation process with $k = 2$ (sample diameter=6mm).

The selected volume within the ore sample was composed by a rich sphalerite zone embedded in the dolomite gangue (Fig. 4.7). This choice enables to analyze and to compare a rich sphalerite zone localized near the center of the image with poor sphalerite zones in the other parts (gangue zones). The Liesegang ring is also perfectly distinguishable on the axial cut of the segmented three-dimensional image presented in Fig. 4.8 (a). Note that the axial term refers to the tomograph rotation axis, i.e. to the rod sample axis. Numerous sphalerite grains with various sizes are found within the gangue showing the interpenetrability of both phases. Strong differences in structure and morphology between rich and poor sphalerite zones are remarkable on radial cuts (Fig. 4.8 (b) and Fig. 4.8 (c)). On the one hand, Fig. 4.8 (b) is a radial plan selected in the Liesegang ring (located by a red line in Fig. 4.8 (a)) and showing an important and apparently continuous sphalerite phase. On the other hand, Fig. 4.8 (c) is a radial plan selected in the gangue zone (located by a blue line in Fig. 4.8 (a)) and showing the discontinuous sphalerite grains that have been mentioned above.
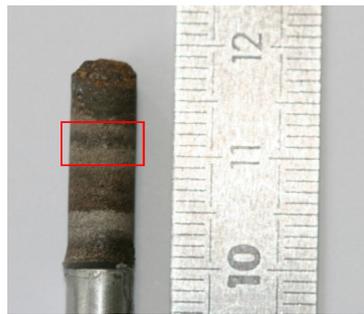
Fig. 4.7 Photography of the ore sample. The zone view by the X-ray tomograph is delimited by a red rectangle.
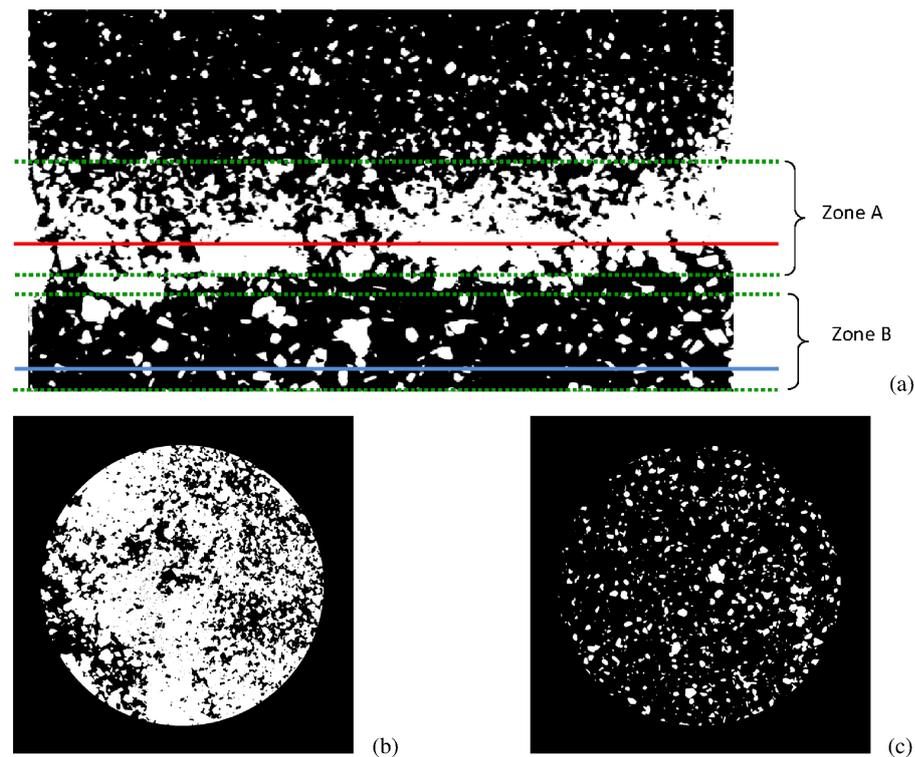

Fig. 4.8 Segmented images of the 3D ore sample (sample diameter=5.3 mm). (a) Axial cut of the 3D image (5.3x3.2 mm^2), (b) 2D radial cut following the red line visualized in (a), (c) 2D radial cut following the blue line visualized in (a). For all three images the sphalerite phase is in white, the gangue is in black.

The evolution of the sphalerite volume fraction along the rod axis is an estimator allowing to quantify this important variability (Fig. 4.9). The sphalerite concentrations rise up to near 70 % in the Liesegang ring and down to between 10 and 20 % in

the gangue zones. Other estimators to characterize the sample are chord length distributions. These latter are stereological tools used to describe the interface between two phases. The chord distribution gives the probability of having a chord length between r and r+dr (see [15] or [21] for more details). Chord distributions can be calculated for each phase in a three-dimensional image; giving a sphalerite chord distribution and a dolomite chord distribution for the present study (Fig. 4.10). Hence, two sub-regions representing the rich sphalerite zone (Liesegang ring) called here after zone A and a poor one (gangue zone) called here after zone B, were selected in order to compare their characteristics. The selected sub-regions, zones A and B, are represented in Fig. 4.8 and Fig. 4.9.

Concerning the gangue zone (B), dolomite and sphalerite chord length distributions present exponential decreases (plots are in a semi-logarithmic representation). This type of porous medium, in which both phases chord distributions are exponential, is called a long-range random medium [15,21]. In other words, both phases in zone B were randomly distributed. The absence of correlation peaks has demonstrated that these phases have not got any favored grain size. Concerning the rich sphalerite zone (A) the analysis is more tricky. Sphalerite chord length distribution presents two exponential decreases, the first one in the [50-225] μm range, the other one in the [350-1200] μm range. This could be attributed to two sphalerite grain distributions with two distinct sizes distributions. The dolomite chord length distribution presents no particular analytical expression (nor exponential decrease nor algebraic formulation) and this is difficult to extract any pertinent information from such data.
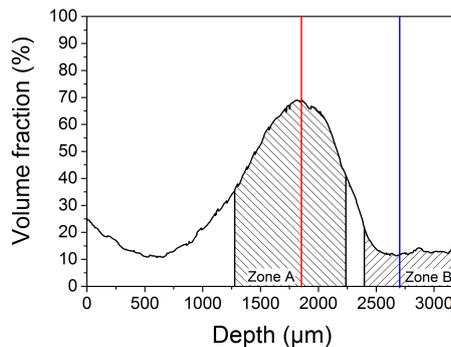
Fig. 4.9 Sphalerite volume fraction along the axial length of the sample. The two zones (A and B) selected for the chord length distribution analysis are represented as well as the two radial plans selected on the axial-cut-mine figure (Fig. 4.8): radial-cut-rich and radial-cut-poor (red and blue line respectively).
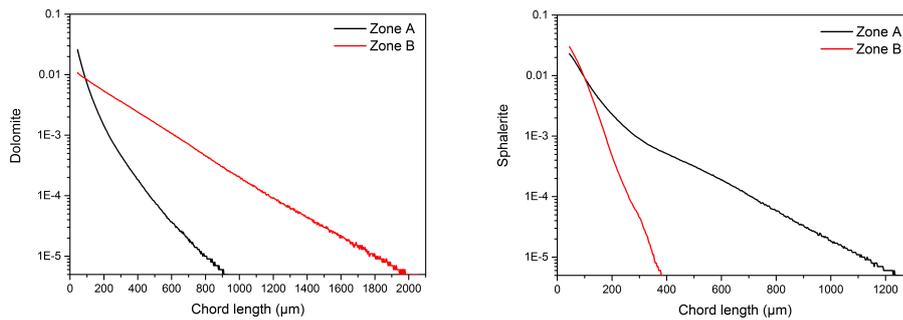
Fig. 4.10 Chord length distributions for the dolomite and the sphalerite phases.

5 Conclusion

It has been shown how a decomposition image preprocessing model may be useful to segment and to perform a structural and morphological analysis of geomaterials. This model is sufficiently adaptable to let the user choose the most relevant image component for each situation. Next issue is to use it for other studies while improving the tuning of parameters with respect to the samples. Indeed, the choice of parameters may give information at different scales that can be useful to give more precise knowledge of the material. Concerning the first case study, the used procedure showed its potential for the three-dimensional characterization of interconnected transgranular crack network in a weathered granite, essential for the understanding of fluid transport and mechanical behavior. However, due to the *low* image resolution, it was not possible to assess the whole microporosity related to the mineral (plagioclase) weathering. This three-dimensional characterization will be done in future studies on smaller samples and using synchrotron facility (voxel size near 0.3 μm). Concerning the second case study, the chosen segmentation process is fully adapted to the ore sample. Indeed, the two main phases (sphalerite and dolomite) are perfectly distinguishable enabling the morphological and structural analysis of this geomaterial. With these binarized images a model to estimate the liberation mesh size of ore samples will be developed. For that purpose, the three-dimensional binarised image of bulk ore will be grind numerically with three-dimensional Voronoi cells up to the liberation mesh size.

References

1. C. Alves, M. A. Sequeira Braga, and C. Hammecker. Water transfer and decay of granitic stones in monuments. *Comptes Rendus de l'Académie des Sciences*, ser.IIa(5):397–402, 1996.
2. C.A.S Alves and M.A. Sequeira Braga. *Decay effects associated with soluble salts on granite buildings of Braga (NW Portugal).* 9. Mineralogical Society of Great Britain & Ireland, 2000.
3. G.G. . Amoroso and V. Fassina. *Stone decay and conservation*. Elsevier, Amsterdam, 1983.

4. L. Barbanson. Relations entre les minéralisations zn-pb de la plate-forme carbonatée urgonienne du domaine ouest-santanderin (nord de l'espagne) et dynamique tectono-sédimentaire. In *MVT Workshop, Mississippi Valley Type Deposits in Europe and North Africa, comparisons with North American Deposits, constraints on modeling paleocirculations*, 1993.

5. M. Bergounioux. Second order variational models for image texture analysis. *Advances in Imaging & Electron Physic*, 181, 2014.

6. M. Bergounioux. Mathematical analysis of a inf-convolution model for image processing. *Journal of Optimization Theory and Applications*, pages 1–21, 2015.

7. M. Bergounioux. Second order decomposition model for image processing : numerical experimentation. In M. Bergounioux, G. Peyré, C. Schnörr, J.-B. Caillau, and T. Haberkorn, editors, *Variational Methods In Imaging and Geometric Control*, volume 17. Degruyter, 2016.

8. M. Bergounioux and L. Piffet. A second-order model for image denoising. *Set-Valued Variational Analysis*, 18(3-4):277–306, 2010.

9. M. Bergounioux and L. Piffet. A full second order variational model for multiscale texture analysis. *Computational Optimization and Applications*, 54(215-237), 2013.

10. A. Chambolle and T. Pock. A first-order primal-dual algorithm for convex problems with applications to imaging. *Journal of Mathematical Imaging and Vision*, 40(1):120–145, 2011.

11. W. Degruyter, A. Burgisser, O. Bachmann, and O. Malaspinas. Synchrotron x-ray microtomography and lattice boltzmann simulations of gas flow through volcanic pumices. *Geosphere*, 6(5), 2010.

12. L.A. Feldkamp, L.C. Davis, and J.W. Kress. Box-skeletons of discrete solids. *Journal of the Optical Society of America A*, 1:612–619, 1984.

13. N. Ferreira, G. Dias, C.A.P. Meireles, and M.A. Sequeira Braga. Carta geológica de portugal na escala 1/50.000. notícia explicativa da folha 5-d braga. In *Departamento de Geologia, Instituto Geológico e Mineiro, Lisboa*. 2000.

14. ISRM. Basic geotechnical description of rock masses. *Int. J. Rock Mech. Min. Sci. & Geomech. Abstr.*, 18:85–110, 1981.

15. D. Levitz, P. Tchoubar. Disordered porous solids: from chord distribution to small angle scattering. *J Phys I*, 2:771–790, 1992.

16. A. Lumpkin, B. Yang, C. Yao, and L. Emery. X-ray imaging of the aps storage ring beam stability effects: from the alaskan earthquake to undulator field changes. *Medical Imaging*, 4:2423–2425, 2003.

17. JMS Matias and C.A.S. Alves. The influence of petrographic, architectural and environmental factors in decay patterns and durability of granite stones in braga monuments (nw portugal). In *Natural Stone, Weathering Phenomena, Conservation Strategies and Case Studies*, volume 205, pages 273–281. Geological Society London, 2002.

18. Y. Nesterov. Smooth minimization of non-smooth functions. *Mathematic Programming, Ser. A*, 103:127–152, 2005.

19. S. Osher, E. Fatemi, and Rudin L. Nonlinear total variation based noise removal algorithms. *Physica D*, 60:259–268, 1992.

20. N. Otsu. A threshold selection method from gray-level histograms. *IEEE Trans. Sys., Man., Cyber.*, 9(1):62–66, 1979.

21. O. Rozenbaum. 3-d characterization of weathered building limestones by high resolution synchrotron x-ray microtomography. *Science of the Total Environment*, 409:1959–1966, 2011.

22. O. Rozenbaum, S. Anne, and J.-L. Rouet. Modification and modelling of water ingress in limestone after application of a bio-calcification treatment. *Construction and building material*, 70:97–103, 2014.

23. O. Rozenbaum, J. Machault, E. Le Trong, Y.G. Ngassa Tankeu, and L. Barbanson. Ore fragmentation modelling for the evaluation of the liberation mesh size. In *13th SGA Biennial meeting*, 2015.

24. M.A. Sequeira Braga, J.E.L. Nunes, H. Paquet, and G Millot. Climatic zonality of coarse granitic saprolites ("arènes") in atlantic europe from scandinavia to portugal. *Sci. Géol. Mém*, 85:99–108, 1990.

25. G. Torraca. Treatment of stone monu- ments: a review of principles and processes. *Conserv Ston.*, 1:297–315, 1983.

26. M.P. Tran. *Denoising 3D medical images using a second order variational model and wavelet shrinkage*. PhD thesis, Orléans, 2012.
27. E. Van de Casteele, D. Van Dyck, J. Sijbers, and E. Raman. The effect of beam hardening on resolution in x-ray microtomography. *Medical Imaging*, pages 2089–2096, 2004.
28. G. Venzl. Pattern formation in precipitation processes. ii. a postnucleation theory of liesegang bands. *J. Chem. Phys.*, 85(4):2006–2011, 1986.
29. P. Weiss, G. Aubert, and L. Blanc Féraud. Efficient schemes for total variation minimization under constraints in image processing. *SIAM Journal on Scientific Computing*, 31(3):2047–2080, 2009.